



# Prediction of primary water stress corrosion crack growth rates in Alloy 600 using artificial neural networks



Jiangbo Shi<sup>a,b</sup>, Jihui Wang<sup>a</sup>, Digby D. Macdonald<sup>b,\*</sup>

<sup>a</sup> School of Materials Science and Engineering, Tianjin University, Tianjin 300072, PR China

<sup>b</sup> Department of Nuclear Engineering, University of California, Berkeley, CA 94720, USA

## ARTICLE INFO

### Article history:

Received 25 October 2014

Accepted 6 December 2014

Available online 12 December 2014

### Keywords:

A. Alloy

B. Modeling studies

C. Stress corrosion

## ABSTRACT

After reviewing of the data for primary water stress corrosion cracking (PWSCC) for Alloy 600 in the literature, a crack growth rate (CGR) database was assembled, and an ANN model was developed and trained upon the data, in order to model PWSCC in Alloy 600. The dependence of PWSCC CGR on each of the principal independent variables of the system has been predicted. Sensitivity analyses were conducted via “fuzzy logic” and the importance of each variable was analyzed and show that IGSCC in Alloy 600 is primarily mechanical in character with the electrochemistry being a significant contributor.

© 2014 Elsevier Ltd. All rights reserved.

## 1. Introduction

Ni-based Alloy 600 has been used widely for steam generator (SG) tubing and penetration nozzles for the control rod driving mechanism (CRDM), and for other pressure boundary components, in pressurized water reactors (PWR), because of its good corrosion resistance. However, there have been many reports of intergranular stress corrosion cracking (IGSCC) in “mill-annealed” Alloy 600 resulting in component failure after long-term operation in PWR primary environments. The first such corrosion mechanism to cause concern in PWRs was IGSCC from the primary side of “hot leg” steam generator tubes in contact with the primary coolant (LiOH/H<sub>3</sub>BO<sub>3</sub> at 290–330 °C), which has become known in the nuclear power industry as primary water stress corrosion cracking (PWSCC). This phenomenon is of great importance, considering the safety issues involved and the costs to the consumer and operator, alike. The problem could be significantly alleviated if a model was available that could precisely predict the crack growth rate (CGR), because then repairs might be affected during scheduled outages, so as to avoid costly, unscheduled outages, the cost of which is not built into the price of the product. However, it is well known that CGR in Alloy 600 is controlled by many properties of the system, reflecting a complex combination of stress, environment, and a susceptible material. It is extremely difficult to study the influences of all possible parameters by independent experiment, due to the difficulty in controlling or even measuring a large number of independent variables simultaneously in the high pressure, high

temperature aqueous environment. Many studies have focused on the establishment of PWSCC models and their use in predicting CGR. Empirical/phenomenological models, including the Scott model [1]; the similar Materials Reliability Program, MRP-55, model [2]; and the MRP-115 model for weld metal [3] have been developed for this alloy/environment system. Recently, a theoretical model known as the Fracture Research Institute (FRI) model has been proposed by Shoji and other researchers from Tohoku University [4]. The FRI model incorporates both electrochemistry and fracture mechanics considerations, although the inclusion of electrochemical factors is somewhat inadvertent in that the model is calibrated on CGR data that are clearly affected by the electrochemistry of the system. The FRI model does not incorporate the electrochemistry of the system explicitly. Thus, none of these models incorporate explicitly electrochemical mechanisms, such as that embodied in the Mixed Potential Model (MPM) for estimating the electrochemical corrosion potential (ECP), or for the purpose of describing ion transport down a crack or within the external environment. However, the coupled-environment fracture model (CEFM), which was developed by Macdonald et al. [5,6] for calculating CGR in sensitized Type 304SS in light water reactor (LWR) coolant environments, does incorporate physico-electrochemical–mechanical factors with emphasis on both the mechanics and electrochemistry of the system. This model, which is based on the differential aeration hypothesis, takes into account both electrochemical and mechanical processes, with crack advance being assumed to occur through the slip/dissolution/repassivation mechanism augmented by hydrogen-induced fracture (HIF), and the basis of this model is a statement of charge conservation and Faraday’s law of charge-mass equivalency. These

\* Corresponding author. Tel.: +1 (814) 360 3858; fax: +1 (510) 643 5792.

E-mail address: [macdonald@berkeley.edu](mailto:macdonald@berkeley.edu) (D.D. Macdonald).

constraints render the model deterministic, due to the fact that the predictions are constrained to “physical reality” by the relevant natural laws.

A major problem in qualifying models for predicting CGR in Alloy 600 (and other alloys) is that CGR data, when shown in two-dimensional plots (e.g., CGR versus extent of cold work or CGR versus temperature), display a dispersion of several orders of magnitude (in some cases up to 3–4 orders of magnitude). This uncertainty arises partly from the failure of many researchers to measure, control, or even report environmental parameters that may have an obvious impact on CGR, such that the matrix containing all the independent variables information is almost always “sparse”. As some of the missing information can be calculated [e.g., conductivity can be calculated from the composition of solution [7] and ECP can be estimated from  $[H_2]$ ,  $[H_2O_2]$ ,  $[H^+]$ ,  $[O_2]$ , temperature, and flow velocity (if known)] using the Mixed Potential Model (MPM) [8], it is postulated that the measured CGR is usually much more accurate than the two-dimensional plots demonstrate. Another issue that needs to be considered is that the apparent dispersion is always so large that it is almost always possible to find data in excellent agreement with any model predictions, so as to “prove” the efficacy of a particular model.

However, unlike the models mentioned above, an ANN model contains no pre-conceived, physico-electrochemical model, but instead seeks to identify and quantify hidden relationships between the dependent and independent variables; in other words an ANN “tells it the way it is”. The main benefits are that prediction results are based purely on data and not on preconceptions, and that the network can extrapolate effects from learned relationships without a mathematical model for extrapolation being specified.

## 2. Artificial neural network model

### 2.1. Introduction of artificial neural networks

Artificial neural networks (ANNs) are computational tools inspired by an animal's central nervous systems (in particular the brain) that are capable of machine learning and pattern recognition. They are usually presented as systems of interconnected “neurons” that can compute values from inputs by feeding information through the network. ANNs have been applied successfully by a number of researchers in the field of corrosion prediction and a few of these prior works are as follows. P.-C. Lu, et al. were the first to use artificial neural networks to study stress corrosion cracking [9,10], in which they applied an ANN to the study of IGSCC in sensitized Type 304 SS in high temperature water at 288 °C. Cai et al. [11], Pintos et al. [12], and Halama et al. [13] studied atmospheric corrosion using ANNs, and through sensitivity analysis, the effects of various factors were demonstrated. Smets and Bogaerts [14] successfully used ANNs for predicting SCC risk in austenitic stainless steels, and for defining the combined effects of three parameters (temperature, chloride concentration, and oxygen content) on the occurrence of SCC in austenitic chromium-nickel stainless steels in high-temperature water. Benhaim and Macdonald [15] applied an ANN to the study of the effect of various parameters on the acidity of simulated geological salt repositories, which contain brine inclusions, and predicted that the pH of the saturated brine inclusions would lie between 3.2 and 5, as the temperature of the repository decayed over thousands of years. All of these studies demonstrated that an ANN is an efficient computational tool for analyzing complex systems, especially when conventional modeling by analyzing specific reactions and processes may be difficult or unfeasible.

#### 2.1.1. Basic elements

As noted above, an artificial neural network (ANN) is a computational tool based on biological neural networks and comprises an

interconnected group of artificial neurons. The schematic of a three-layer neural network is shown in Fig. 1(a). Each layer consists of one or more neurons, as defined in Fig. 1(b). Each neuron in the first layer (also known as the input layer) receives a user specified input vector, processes the input vector and generates an output value. The output values from this layer are then passed on as inputs to each neuron in the next layer. The output values from the last layer (known as the output layer) correspond to the quantities that we need. The layers between the input and the output layers are termed “hidden layers”.

Mathematically, the output of the  $k_{th}$  neuron in the  $l_{th}$  layer receiving a  $n$ -dimensional input vector is expressed as the following equation:

$$y_k^{(l)} = f \left( b_k^{(l)} + \sum_{i=1}^n w_{k,i}^{(l)} x_i^{(l)} \right) \quad (1)$$

where  $y_k$  is the output of the  $k_{th}$  neuron from an input vector  $x = (x_1, \dots, x_n)$ , with  $x_i$  representing the input parameters. The  $w_{k,i}^{(l)}$  values are the weights, which are used for scaling the respective input value to the neuron. Thus, within each layer, these weights indicate the relative importance of the parameters. The parameter  $b_k$  is termed the bias, which is used to account for the contribution of the unknown, but influential parameters, that have not been included in the analysis, most likely because of the lack of relevant data. The bias is much like a weight, except that its value is determined during the training of the net and is independent of the weighted inputs from the neurons from the previous layer (see Fig. 1). Its function is to modify the output, as indicated in Eq. (1). The weighted sum of the inputs and the bias value are passed through the transfer function  $f$ , which produces the scalar output. The establishment of the weights essentially imbues the net with “memory” and enables the relationships between the **output (CGR)** and each of the independent **input variables (temperature, ECP,  $K_i$ , conductivity, pH, boron content, lithium content and extent of cold work)** to be defined. In this study, a **hyperbolic tan (tanh) function** has been used as the **transfer function** in the **hidden** layers, while a **linear function**, rather than a sigmoid function, as used for the hidden layers, has been **used for output layer**.

#### 2.1.2. Architecture

The number neurons in the input and output layer effectively represents the number of variables used in the prediction and the number of variables to be predicted, respectively. The hidden layers act as feature detectors and, in theory and practice, there is generally more than one hidden layer. However, universal approximation theory suggests that a network with a single hidden layer with a sufficiently large number of neurons can interpret any input-output structure [16]. The critical aspect is the choice of the number of neurons in the hidden layer. More hidden neurons result in a longer training period, while fewer hidden neurons provide faster training at the cost of having fewer feature detectors.

#### 2.1.3. Training

Once the architecture of an artificial neural network and the network weights and biases are initialized, the network is ready for training. The training process of an ANN involves tuning the values of the weights and biases of the network to optimize the performance of network, which is judged by the mean squared error ( $\sigma$ ) defined below. The general objective is to make output  $t_i$  and input  $a_i$  identical for  $i = 1, 2, \dots, n$ .

$$\sigma = \frac{1}{N} \sum_{i=1}^N (e_i)^2 = \frac{1}{N} \sum_{i=1}^N (t_i - a_i)^2 \quad (2)$$

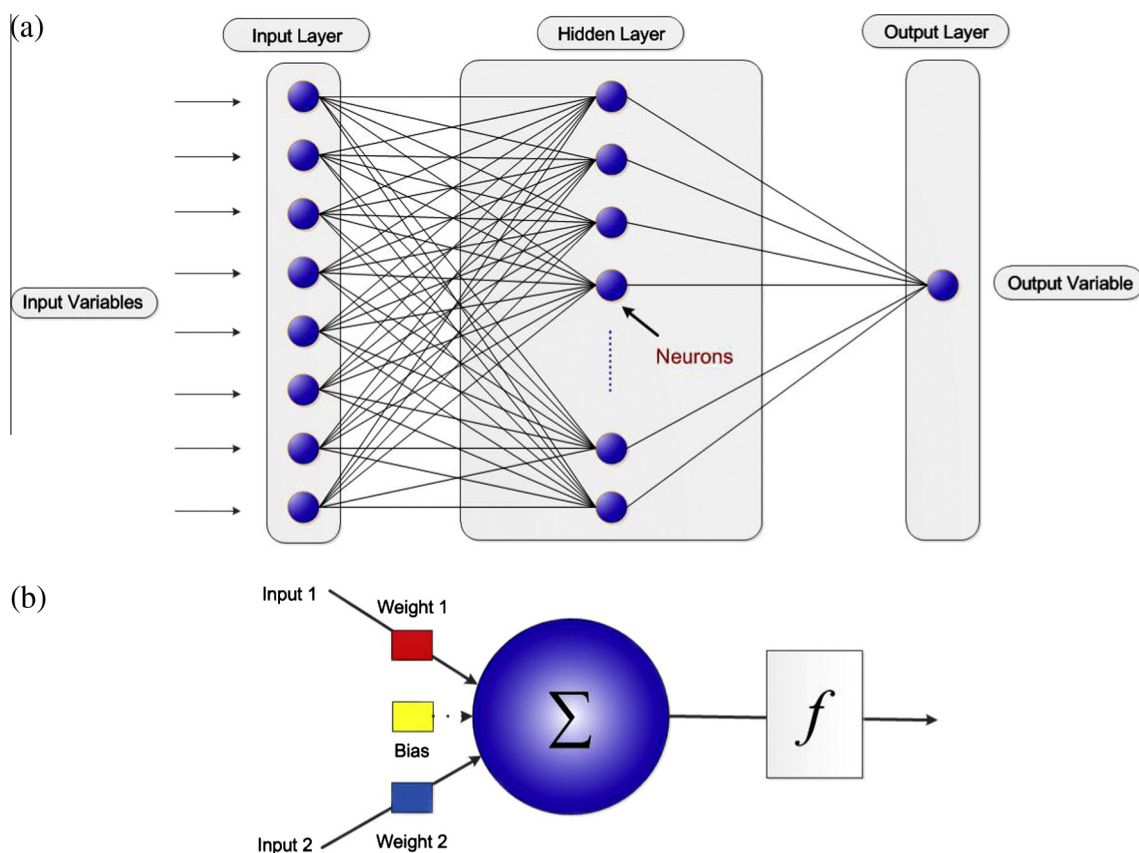


Fig. 1. (a) A schematic of a three-layer neural network and the (b) schematic of each neuron in the network.

The nonlinear nature of the aforementioned error function makes it non-convex and prone to have local optima. The **Levenberg–Marquardt back propagation algorithm** is often used as a **training function**. In this algorithm, following the **initialization of the network weights and biases**, the **training proceeds in the direction contrary to the error function gradient thus ensuring a lower error value**. This procedure continues until the minimum error is reached or some other termination criteria are met.

## 2.2. ANN modeling process

In general, the ANN modeling process used in this study may be described in the following **four stages**: (1) **preparation and preprocessing of the original data set**; (2) **partitioning of the preprocessed data set into learning, validation, and test sets**; (3) **establishing ANN architecture, training, and testing**; and (4) **implementation**.

### 2.2.1. Preparation and preprocessing of the original data set

As database generation is a critical step for designing an accurate network, following a literature survey, we collected 163 experimental data related to CGR of Alloy 600 from different resources. Some of these data were from published paper [17–20] and the others from technical reports [21–25]. All the data collected were from experiments that did not employ SSRT (slow strain rate test) or CERT (constant extension rate test) techniques for detecting IGSCC, due to the experiments performed using SSRT or CERT cannot control the number of cracks for a given area and do not differentiate between the crack initiation and propagation stages. Therefore, these data are not appropriate for enquiring into CGR alone.

There is a serious non-integrity of the information contained in the data resources. Thus, not every experiment was performed at the same conditions, or with the same controlled variables. Some important variables, which may have obvious effect on CGR were not measured or reported at all. Generally, the data base has five common variables:  **$T$**  (temperature),  **$K_I$**  (stress intensity factor), **extent of cold work**, and the **B** and **Li** contents of the solution, with the **electrochemical corrosion potential (ECP)** being essentially pegged at a value reflecting the high hydrogen content frequently employed, in order to simulate PWR primary coolant environments. In order to unify the experimental data base with data being taken from different sources, we identified three more important variables in describing PWSCC and calculated those variables from the available information contained in the original studies. Thus, following on from our previous work on modeling CGR in sensitized Type 304 SS in BWR coolant environments, using both ANNs [9,10,34] and deterministic physico-chemical models (the CEFM [5,6]), we identified that, in addition to temperature, stress intensity factor, extent of cold work (as reflected in the yield strength), B (as  $H_3BO_3$ ) content, and Li (as  $LiOH$ ) content in the solution, other important variables included the ECP, pH, and solution conductivity ( $\kappa$ ). Other independent variables, such as  $H_2$  fugacity, and irradiation effects (IASCC) were deemed to be important, but the scarcity of data precluded their inclusion in the current database. More details concerning the calculation of ECP in PWR environments and conductivity are given elsewhere [7]. The conductivity values generally reported in the literature were ambient temperature values and did not refer to the operating temperature (e.g. 330 °C) at which the crack grows. Because the conductivity of an electrolyte changes dramatically with temperature, we calculated the conductivity corresponding to the test temperature from the solution composition and ion

conductance versus temperature data and used this value as the input parameter to train the ANN [26]. Table 1 shows the selected input parameters for the ANN developed in this work.

Pre-processing the original data set is another important step before training the neural network, in that the original data set must be normalized to avoid the dominance of one parameter that has a large value. All samples were normalized to the range [0...1] by dividing each by that with the highest value, so that they conformed to the demands of the transfer function used (sigmoid function) in the building of the ANN. The data sets ( $x_i$ ) were scaled to a new value  $\hat{x}_i$ . This was done using the formula [16]:

$$\hat{x}_i^{(m)} = \frac{x_i^{(m)} - \min_{n=1,N}\{x_i^{(n)}\}}{\max_{n=1,N}\{x_i^{(n)}\} - \min_{n=1,N}\{x_i^{(n)}\}} \quad (3)$$

### 2.2.2. Partitioning the data set

The scaled database from pre-processing conducted in the previous step, was randomly divided into three parts: a training set (70%), a validation set (15%), and a test set (15%). The training data were directly used for training the network. During training, the process was monitored by evaluating the validation data. In other words, the validation set serves to determine the termination of the training procedure if there is no improvement in the prediction capabilities of the network, as determined by comparison with experiment ("training set"). Finally, once the network was fully trained, the test data ("test set") that had not been used in the training process was employed to validate the predictive capabilities of the network.

### 2.2.3. ANN model architecture setting, training and testing

As noted above, the number of nodes in the input and output layers are set by the number of input variables (eight) and the number of variables to be predicted (one, the CGR). Only the number of hidden neurons needs to be established; based on the training performance of different networks containing different numbers of nodes we chose 25 hidden-layer nodes, which gave the best performance, as judged by the minimal  $R^2$ . The training proceeds in an iterative manner. For a given set of initial weights, the learning process was stopped when the mean square error in the validation data set began to grow for a certain number of iterations in the optimization procedure. The best set of weights was the one with the lowest mean square error and relative good performance on the validation data set. The test set error is not used during training, but it is applied to the network to validate the prediction capabilities of the network. A comparison between the experimental values of CGR and the ANN predicted values is plotted in Fig. 2(a). If the data were ideal and the ANN was of high fidelity, the experimental versus predicted values should fall on the diagonal line of 45° slope. Although there are some significant scatter of the data points, reflecting uncertainty in the original database (i.e., in both the independent and dependent variables), the predicted CGR obtained from the training set (85% of the total)

is in good agreement with the experimental data. The  $R$ -squared value for the correlation was 0.98. This indicates that the ANN has achieved a high level of correlation. The indicated 95% confidence level uncertainty ( $\pm 0.3$  log units in CGR) is best regarded as being the inherent accuracy of the measured crack growth rate, which is considerably lower than the 3 orders of magnitude scatter observed in a plot of CGR versus  $K_I$  [27] [see Fig. 2(b), for example]. This inherent uncertainty is only slightly less than that observed in CGR data for IGSCC in sensitized Type 304 SS in simulated BWR coolant (pure water at 288 °C), as determined by our recent ANN analysis [28]; a finding that is not surprising given that most of the CGR data for both systems were measured using the same DC potential drop technique. In our opinion, the scatter observed in Fig. 2(b) is an artifact of attempting to represent multi-variate data (of 8 dimensions, in our present case) on a two-dimensional plot without constraining the values of the remaining seven independent variables. If the scatter displayed in Fig. 2(b) represented the inherent accuracy, then, clearly, the data would be worthless from an engineering viewpoint.

### 2.2.4. Implementation

The best-trained ANN net was used to predict the CGR under different sets of assumed conditions. As an ANN can account for the dependent variable/independent variable relationships, the net, therefore, allows us to ascertain the behavior of CGR with respect to the variation of each variable independently or in combination.

### 2.3. Sensitivity analysis

As ANNs are purely empirical models, they are often criticized for their inability to inherently produce a mechanistic understanding of the process being modeled. Therefore, ANNs are often referred to as being "black boxes" that have no mechanistic awareness and develop no mechanistic understanding [29]. However, this may not be the case if the architecture of an ANN is properly set, or if the model inputs and outputs are carefully and rigorously scrutinized. By ranking input parameters based on their significance to correctly predict the output value, one can determine which parameter is most important in predicting PWSCC CGR and hence specify the "character" of the phenomenon (crack growth in Alloy 600 in PWR primary coolant). This is important, because a viable physic-chemical model should reflect the same character. This process of determining the "character" of a process is essentially a form of sensitivity analysis.

Sung [30] compared three different methods for ranking input importance: sensitivity analysis, fuzzy curves, and change of mean square error; and has analyzed their effectiveness. According to his findings, the fuzzy curves method is more effective than sensitivity analysis or the mean square error method, in most cases. Furthermore, this technique has been used in previous corrosion studies [31–33].

The fuzzy curves method of Lin and Cunningham [34] uses fuzzy logic to establish the relationship between the input variables and the output variable. Suppose a system has  $N$  inputs  $X = (x_1, x_2, \dots, x_N)$ , and one output  $Y = (y)$ , and the number of training patterns (or training data points) is  $P$ . The fuzzy curve is generated by using the Gaussian function:

$$\varphi_{ik}(X_i) = e^{-\left(\frac{x_{ik} - x_i}{b}\right)^2}, \quad k = 1, 2, \dots, P; \quad i = 1, 2, \dots, I \quad (4)$$

where  $\varphi_{ik}$  is the membership function used to form the fuzzy curve for each input candidate,  $x_i$  in the  $k$ th pattern. According to Lin and Cunningham [34], a fuzzy curve ( $C_i$ ) for each input ( $x_i$ ) can be constructed by using the center of the area method for "defuzzification":

**Table 1**  
Inputs selected for the artificial neural network.

Inputs	Range
Temperature	290–360 °C
$K_I$	4.6–101 MPa $\sqrt{\text{m}}$
pH	5.52–9.19
Conductivity	1.7–1116 $\mu\text{S}/\text{cm}$
ECP	–1.096 $V_{\text{she}}$ to –0.61 $V_{\text{she}}$
Yield strength	211–500 MPa
$\text{B}(\text{OH})_3$	0–1800 ppm
LiOH	0–10 ppm



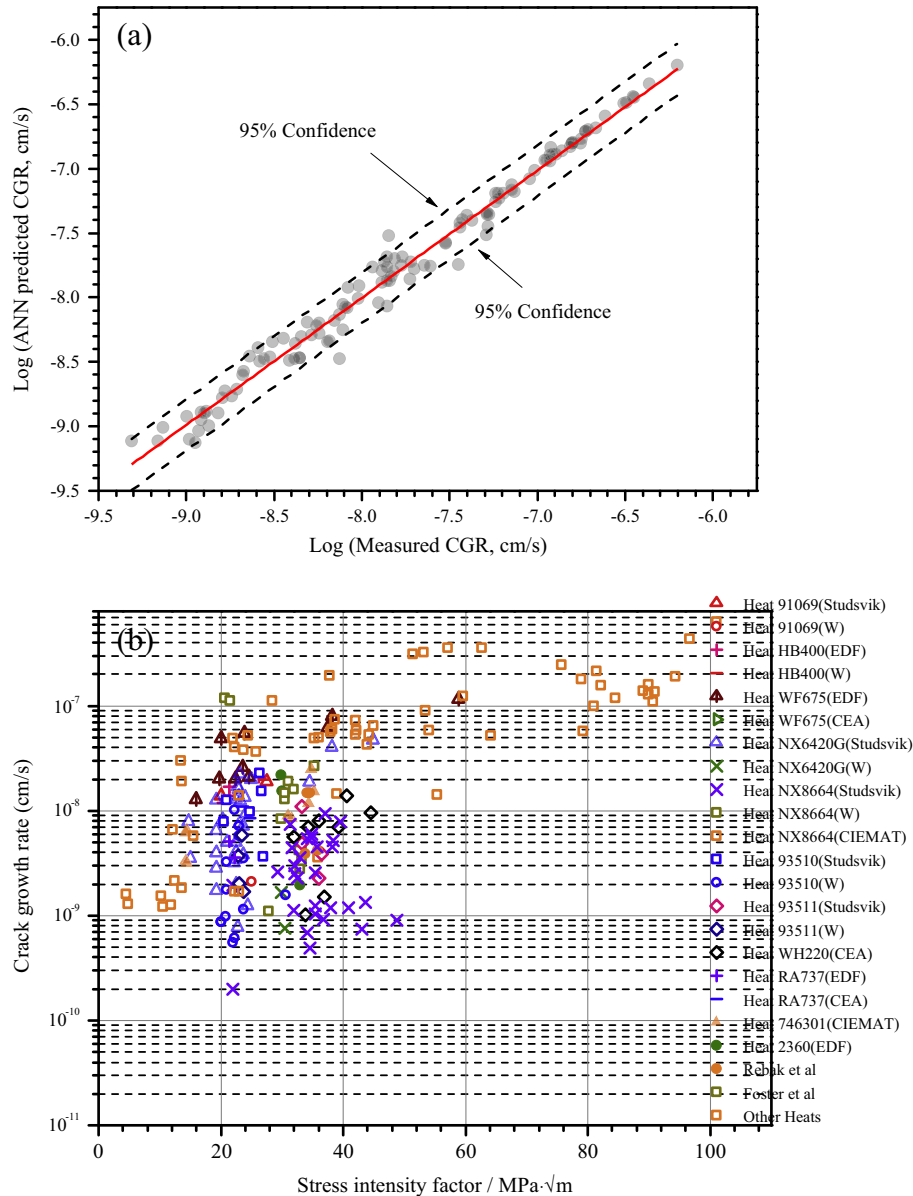


Fig. 2. (a) ANN-predicted versus measured CGR during training of the ANN. (b) Screened laboratory data shows the dependence of CGR on  $K_I$ .

$$C_i(x_i) = \frac{\sum_{k=1}^P \varphi_{ik}(x_i) y_k}{\sum_{k=1}^P \varphi_{ik}(x_i)} \quad (5)$$

where in the plot the fuzzy curve in  $x_i - C_i(x_i)$  space, the input significance is related to the range the fuzzy curve spans on the C-axis. Large ranges indicate larger spans and greater significance. Conversely, smaller ranges indicate smaller spans and lower significance.

Table 2 shows the significance of each input numerically as a “range”. These ranges represent the span of the fuzzy curves. As may be seen, the input variables are ranked as follows:  $T > K_I > \text{ECP} > \kappa > \text{Li content} > \text{pH} > \text{yield strength} > \text{B content}$ . Note that the yield strength should have a major impact on CGR; however, it lies second to last in this list, this is possibly due to the limited range (211–500 MPa) of yield strength in our database. Generally, this ranking agrees well with some other researcher’s results [35–37], which demonstrate that temperature and stress intensity factor have obvious effects on the CGR, while water chemistry has a lower impact on the CGR. Also can be seen from Table 2, both the

Table 2

Input parameters ranked according to their significance in determining CGR.

Rank	Input parameter	Range
1	Temperature (°C)	1.7983
2	$K_I$ (MPa √m)	1.4733
3	ECP (V <sub>she</sub> )	1.4026
4	Conductivity(μS/cm)	1.3683
5	Li (ppm)	1.362
6	pH	1.1577
7	Yield strength (MPa)	0.7379
8	B <sub>3</sub> (OH) <sub>3</sub> (ppm)	0.386

principal mechanical factor ( $K_I$ ) and the principal environmental factor (ECP) have a major impact on CGR, but the mechanical factor contributes more to CGR. Accordingly, IGSCC in mill-annealed Alloy 600 may be described as being “environmentally-assisted mechanical” in character. This is different from the phenomenon of IGSCC in sensitized Type 304 stainless steel, while the contribution to CGR from the environmental factor is larger than that of

mechanical factor [38]. In the most viable of mechanisms for crack advance, the mechanical processes occurring at the crack tip, such as strain and strain-induced fracture, are strongly coupled with the electrochemical processes, such as metal dissolution and hydrogen injection into the matrix ahead of the crack tip, subsequently followed by hydrogen-induced fracture. Thus, the rate at which this coupled process can occur will be determined by both mechanical and electrochemical parameters. For example, in the case of IGSCC in sensitized Type 304 SS in high temperature water, and noting that the CGR is the product of the microfracture frequency (a mechanical process) and the microfracture dimension, which in turn appears to be determined by hydrogen induced fracture, and is essentially electrochemical in nature, it is the microfracture dimension that controls the CGR and we designate fracture in that alloy as being essentially “electrochemical in nature”. In the case of Alloy 600, it appears that the mechanical processes dominate, but it is hard to be unequivocal on this issue, because we do not have the benefit of the coupling current measurements that we had in the case of Type 304 SS. Thus, the classification is made solely upon the basis of the significance of the independent variables.

### 3. Results and discussion

The ANN developed in this study for predicting PWSCC CGR of Alloy 600 as a function of relevant independent variables ( $T$ ,  $K_I$ , Yield strength, Li content, B content ECP and pH) captures the well-known nonlinear interactions between the CGR and some of the most important variables, as illustrated in Figs. 3–10. In general, each figure depicts the SCC behavior as a function of one of the input parameters; the remaining independent variables being maintained constant within relevant ranges or, if they are function of the variable under consideration, at values calculated according to the specified test conditions.

#### 3.1. Influence of temperature on CGR

According to the data in Table 2, temperature is the principal factor influencing CGR in Alloy 600 in PWR primary coolant under the reactor operating conditions. The logarithm of the predicted CGRs ( $\dot{a}$ ) are plotted as a function of  $1/T$  for different stress intensity factors in Fig. 3, with the relationship being defined as

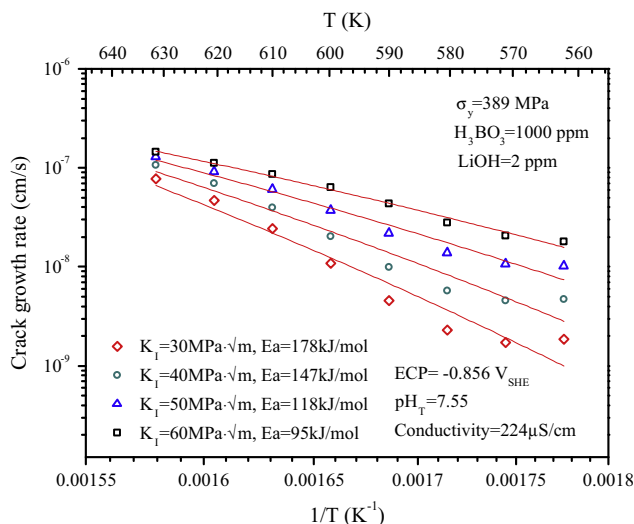


Fig. 3. Effect of temperature on crack growth rate in Alloy 600 in PWR primary coolant as a function of stress intensity factor.

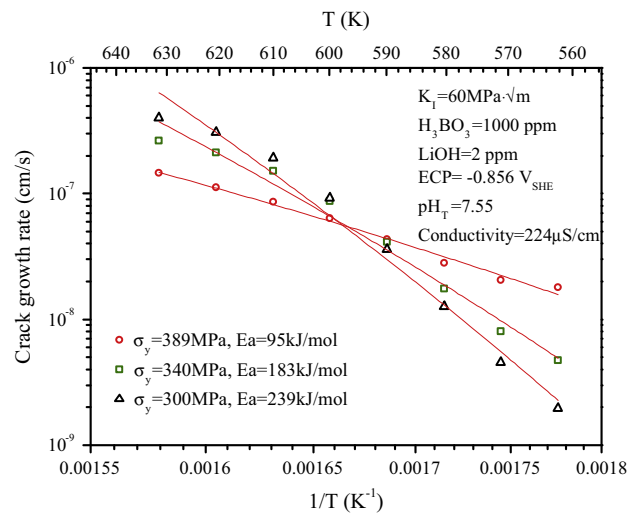


Fig. 4. Effect of temperature on the crack growth rate in Alloy 600 in PWR primary coolant for different values of yield strength.

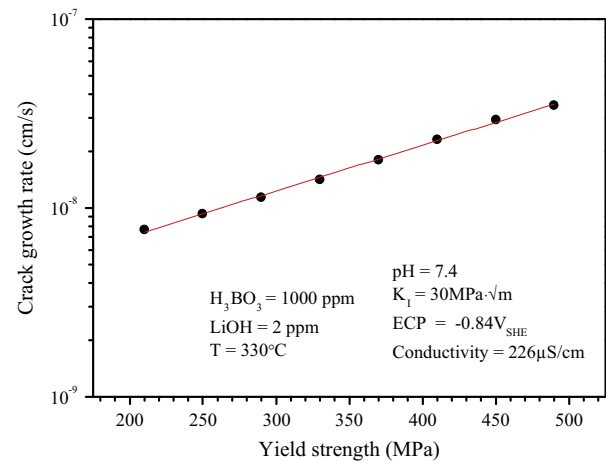


Fig. 5. Effect of yield strength on the crack growth rate in Alloy 600 in PWR primary coolant.

$$\dot{a} = A \cdot \exp(-Q/RT) \quad (6)$$

Eq. (6) yields thermal activation parameters ( $Q$ ), which are obtained using the least square method, of 178 kJ/mol, 147 kJ/mol, 118 kJ/mol and 95 kJ/mol for  $K_I$  values of 30 MPa  $\sqrt{m}$ , 40 MPa  $\sqrt{m}$ , 50 MPa  $\sqrt{m}$  and 60 MPa  $\sqrt{m}$ , respectively.  $A$  in Eq. (6) is a coefficient. Note that we do not identify  $Q$  with being an “activation energy”, because of the ambiguity in defining exactly what is being “activated” (the ambiguity lies in defining a “mole of cracks”). These results demonstrate that  $Q$  decreases with increasing stress intensity factor. This trend agrees well with Shen and Shewmon’s results [39], who have also demonstrated that CGR is strongly dependent on the void spacing,  $b$ . Under high stress intensity conditions, the strain and strained region around the crack tip are larger, “ $b$ ” would become independent of temperature, and one might expect that the nucleation of a void might be easier, such that the CGR eventually would be limited by the rate of void growth. However, at low stress intensity, the plastic strain and the strained volume in front of the crack tip are expected to be lower, and void nucleation become more difficult. Under these conditions, the nucleation rate might be limiting and  $Q$  would represent the thermal activation for bubble nucleation. With increasing stress intensity, the stress normal to a cavitating grain boundary increases, which decreases the free energy

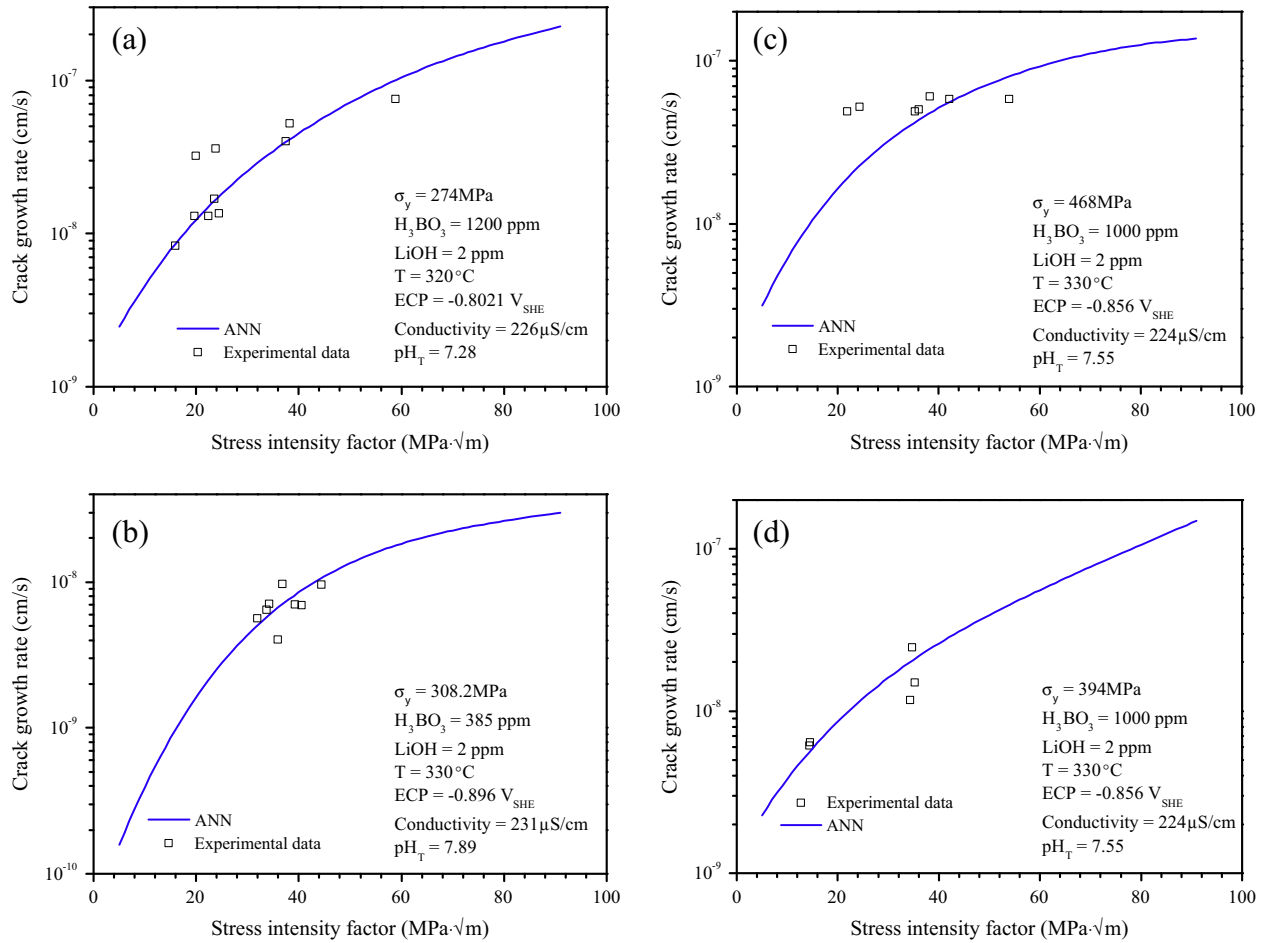


Fig. 6. (a–d) Crack growth rate versus stress intensity factor for Alloy 600 in PWR primary coolant for four different test conditions.

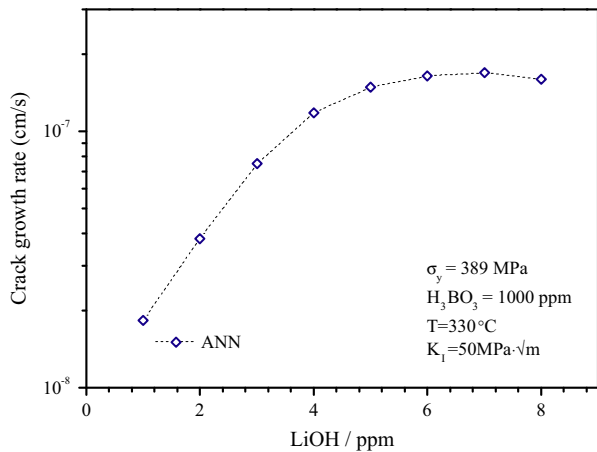


Fig. 7. Effect of lithium content on the crack growth rate of stress corrosion cracks in Alloy 600 in PWR primary coolant.

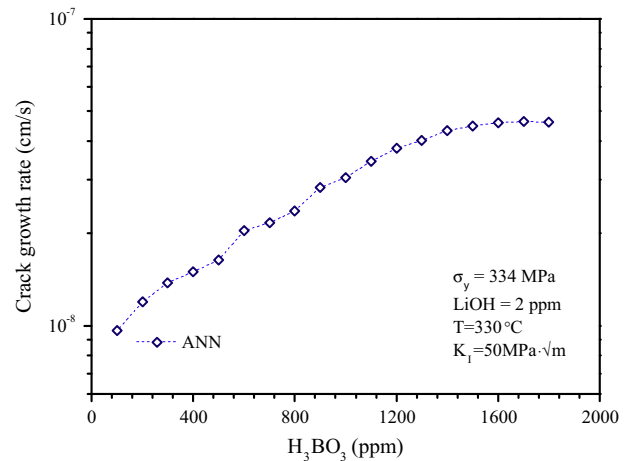
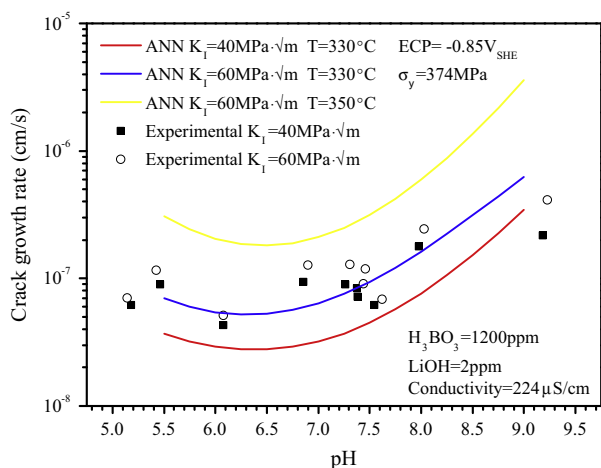


Fig. 8. Effect of boron content on the crack growth rate of stress corrosion cracks in Alloy 600 in PWR primary coolant.

needed to stabilize a critical void nucleus, and the nucleation rate will be drastically increased; this is the reason why  $Q$  decreases with increasing  $K_I$ .

Fig. 4 shows the temperature dependence of the CGR in cold-worked Alloy 600 having different yield strength values. As can be seen from the figure,  $Q$  decreases from 239 kJ/mol to 183 kJ/mol and then to 95 kJ/mol when the yield strength increases from 300 MPa to 340 MPa and then to 389 MPa, respectively. Estimated

thermal activation parameters always include CGR measurement errors, but the trend of an apparent activation parameter decrease with increasing yield strength or extent of cold work has been reported by Rebak [40], Moshier and Brown [41], Terachi [42], and Cassagne and Gelpi [43]. An alloy is cold-worked when it is deformed plastically at temperatures that are low relative to its melting point. Work hardening increases strength, hardness, and



**Fig. 9.** Effect of pH on the crack growth rate of stress corrosion cracks in Alloy 600 in PWR primary coolant.

electrical resistance, while it decreases ductility. Cold work can also increase the dislocation density in a metal. The free energy of a deformed metal is greater than that of an annealed metal, mainly because of the stored strain energy. The effect of yield strength or cold work on the increasing susceptibility of Alloy 600 to cracking can be attributed to two causes (i.e., electrochemical and mechanical). From the electrochemical point of view, it is known that a cold-worked material with high yield strength becomes more active toward electro-dissolution than the same annealed material with low yield strength. Furthermore, the cold-worked material exhibits a lower  $E_{\text{corr}}$  and higher dissolution currents. Therefore, a micro-galvanic cell can be established between the highly strained region and the rest of the non-deformed region. From the mechanical viewpoint, a cold worked material has a higher yield strength and lower ductility. Both factors contribute to a lower resistance to stress corrosion cracking, either by increasing the pre-exponential factor or by lowering activation parameter, resulting in a higher rate of crack propagation as described by Arrhenius equation. The MRP-55 model uses 130 kJ/mol as thermal activation parameter for crack growth rate, which lies between the range of our study, however, it does not take into account the effect of stress intensity factor and yield strength on the thermal activation parameter for crack growth rate. There is other evidence in support of the thermal activation parameter being dependent on both stress intensity factor and yield strength [44,45]. However, this dependence has been largely overlooked by the PWR materials community.

It is important to note that a artificial neural network uncovers the hidden relationships in a multivariate database between the dependent and independent variables without imposing a preconceived model or expectation. Because the ANN uncovered the relationship that the thermal activation parameter,  $Q$ , decreases with increasing  $K_I$  and yield stress, which is sharply at odds with the CGR equation put forth in MRP-55, then that is what the data are telling us, and we must conclude that MRP-55 needs to be modified.

### 3.2. Influence of yield strength on CGR

Fig. 5 illustrates the influence of yield strength on the CGR in Alloy 600. The other input parameters for the ANN are shown in the figure. It is apparent from this figure that an increase in yield strength from 200 MPa to 500 MPa can increase the CGR by more than a factor of five. A comparable enhancement effect of yield

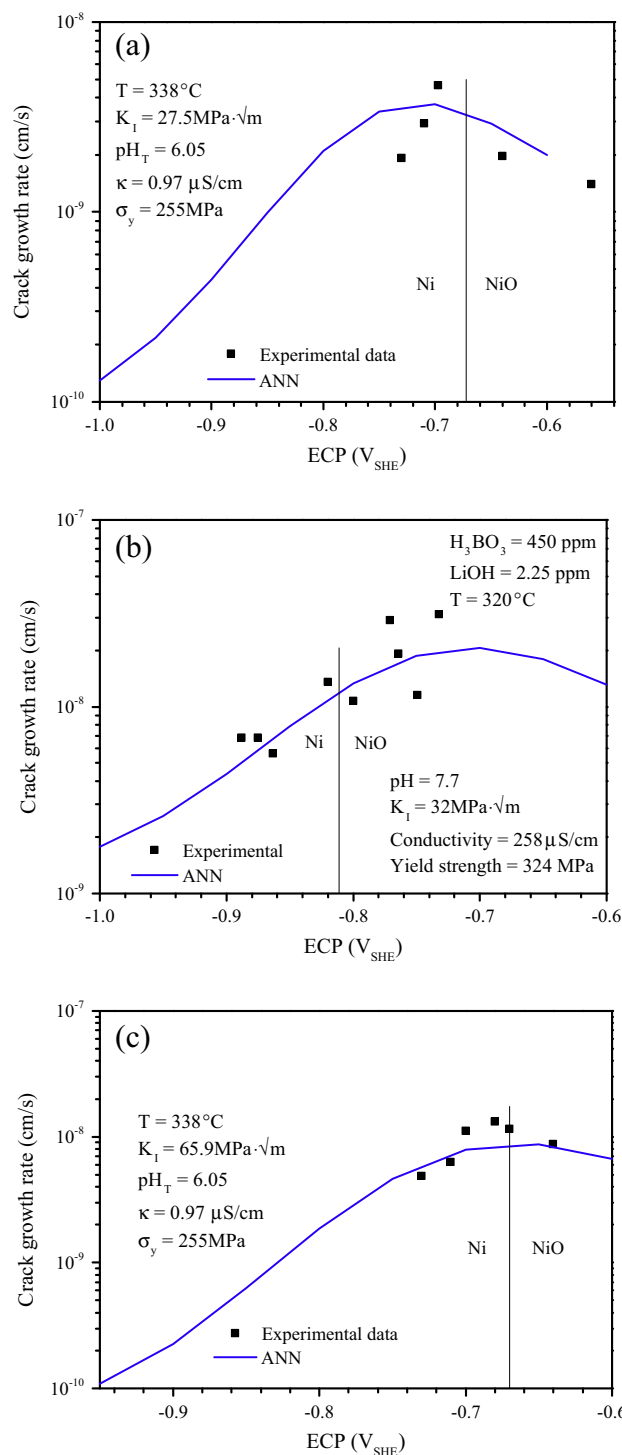


**Fig. 10.** (a–c) Effect of ECP on the crack growth rate of stress corrosion cracks in Alloy 600 in PWR primary coolant.

strength on CGR for stainless steels in both BWR and PWR conditions is also well-documented [35,46–48]. Furthermore, Mosher [49] measured the CGRs of Alloy 600 by bolt load tests and active load tests and found the CGRs could be expressed using the yield strength as a power law with the exponent lying between 2 and 3.4. The proposed effect of the yield strength appears to lie in constraining the plastic zone size at the crack tip to smaller dimensions at a given stress intensity, which gives rise to steeper strain gradients near the crack tip [35,50,51].



### 3.3. Influence of stress intensity factor on CGR

Stress intensity, as well as temperature and yield strength, can exert a major influence on the growth rate of stress corrosion cracks in nickel alloys. It is well known that, when CGR is represented as a function of  $K_I$ , the curve usually comprises three regions [52]. In the first and third regions, CGR depends strongly on  $K_I$ , and very little on solution chemistry. However, in the second region, CGR is virtually independent of  $K_I$ , but is dependent on environmental factors (aggressive anions, temperature, conductivity, etc.) [18]. The CGR is generally induced by the applied stress intensity factor ( $K_I$ ) and the apparent  $K_I$  dependence of the CGR is often empirically described by the following relation [42,53]:

$$\text{CGR} \propto K_I^\beta \quad (\beta = 0.6\text{--}3.2) \quad (7)$$

where  $\beta$  is a constant that describes the  $K_I$  dependence.

Fig. 6(a)–(d) shows the ANN-predicted dependence of CGR on  $K_I$  under different sets of conditions. Generally, the CGR and  $K_I$  exhibits a power law relationship, and at stress intensities higher than about 40 MPa  $\sqrt{\text{m}}$  the CGR curves tend to be less affected by stress intensity and often exhibits a plateau. Some of the experimental data [54] are also shown in the figure, and are seen to be in good agreement (within experimental uncertainty) with the predicted curves. These results demonstrate that the ANN captures in high fidelity the well-known dependence of CGR on  $K_I$  for the different test conditions. And this power law dependence of CGR on  $K_I$  has also been predicted by the MRP-55 model.

### 3.4. Influence of Lithium, Boron and pH on CGR

Figs. 7–9 show the effect of lithium (as lithium hydroxide [LiOH]), boron (as boric acid [H<sub>3</sub>BO<sub>3</sub>]) and pH on CGR in Alloy 600. Thus, Fig. 7 shows the CGR as a function of Li content. It is apparent that an increase in the CGR occurs with increasing Li content, but at lithium contents above 5 ppm (by weight) the CGR reaches a plateau. As the solution conductivity is controlled significantly by the [Li<sup>+</sup>] [55], it is apparent that the initial increase in Li content contributes to the increase in the solution conductivity, which increases the throwing power of the current from the crack growth mouth, such that a larger area on the external surface may contribute to the annihilation of the coupling current (CC) via the redox reactions that occur on the surface. However, when the conductivity increases to a certain value, the CGR becomes independent of the conductivity, because the controlling step is the kinetics of the redox reactions that occur on the external surface.

Fig. 8 indicates that there is a smaller effect of the B content on the CGR in the region from 100 to 1800 ppm. Rebak [17,18], also found that the CGR was not dependent on boric acid concentration, because boric acid is a weak acid and it becomes weaker as temperature increases. Furthermore, it is concluded that the influence of the solution chemistry on the CGR at the higher stress intensities is due to the solution pH, rather than by the presence of Li or B, *per se*, in the solution.

Fig. 9 shows the CGR as a function of the solution pH for stress intensities of 40 and 60 MPa  $\sqrt{\text{m}}$ , and for temperatures of 330 °C and 350 °C. Generally, there is only a slight influence of the solution pH on the CGR, and the CGR reaches a minimum at the neutral point for the temperature of interest (330 °C). The Coupled Environment Fracture Model (CEFM) indicates that the CGR is controlled by the rate(s) of the cathodic reaction(s) that occur on the external surface, because the CGR cannot occur any faster than the coupling current can be consumed by these reactions. The rates of these reactions (reduction of oxygen and/or hydrogen evolution) are pH-dependent [56], and it is this dependence that is postulated to be reflected in the observed CGR data for Alloy 600. Also of possible significance

is that the minimum in CGR coincides well with the minimum solubility of Ni, Cr, and Fe oxides in aqueous solutions at 300 °C [57]. The CGR increases in the alkaline region and is more pronounced at 60 MPa  $\sqrt{\text{m}}$  and 350 °C than at the other conditions. The experimental data from Rebak [17] are also shown in Fig. 9; the ANN predictions are in good agreement with the experimental data. The MRP-55 model shows no significant effect of pH on crack growth rate between pH values of 5 and 7.5. However, for solutions of higher pH, there is an observed increase in CGR with increasing pH. This dependence of CGR on pH agrees well with our findings.

### 3.5. Influence of ECP on CGR

Fig. 10(a)–(c) shows the ANN-predicted dependence of CGR on ECP, all the other input parameters are as indicated in the figure. As can be seen from Fig. 10(a)–(c), the CGR increases with increasing ECP up to a maximum value, after which the CGR slightly decreases. Generally, ECP has positive impact on the CGR, and for the whole range of ECP we have studied, the CGR increases by more than an order in magnitude. This results agree well with the sensitivity analysis result, in which the ECP comes out as the third most important parameter in determining the CGR after temperature and  $K_I$ . The experimental data from Refs. [20,58] are also shown in the figure, and there is excellent agreement between the ANN-predicted results and experimental data. It should be noted that in Fig. 10(b), all of the experimental data were calibrated to 320 °C using activation parameter of 130 kJ/mole [59]. The ECP values corresponding to the experimental data were calculated based on the experiment test conditions using Mixed Potential Model (MPM). Morton and his colleagues [20,60] have studied the effect of H<sub>2</sub> fugacity on SCC in nickel-base alloys and found that the peak in SCC growth rates occurs approximately at the Ni/NiO equilibrium potential. This effect has been described fundamentally by the extent to which the alloy's corrosion potential deviates from the equilibrium potential of the Ni/NiO reaction. Judging from the results we have obtained using the ANN over the whole ECP range we have studied, a good correlation between CGR and the equilibrium potential for Ni/NiO can be seen in Fig. 10(a) and (c), but not in the case of Fig. 10(b). Furthermore, upon carefully analyzing the data from which the claims are based, it is apparent that the range in CGR is of the same order as the inherent accuracy of the data as established in this ANN analysis (i.e.,  $\pm 0.3 \log(\text{CGR})$  units).

Finally, it is important to recognize that the purpose of an ANN, as it is used here in the pattern recognition mode, is to uncover hidden relationships in aggregated databases and that it does this more efficiently than human examination. Thus, it is concluded that the relationship between the CGR and the Ni/NiO equilibrium line is not sufficiently strong to be recognized. If so, it may well be unimportant, which is essentially our conclusion.

## 4. Summary and conclusions

The findings of this research may be summarized as follows:

1. An artificial neural network (ANN) for predicting PWSCC CGR in Alloy 600 is described. Based on the experimental data, missing independent variable values (pH, ECP,  $\kappa$ ) were estimated using ancillary models to develop a comprehensive database for training the ANN. The ANN involves pre-processing and partitioning of the experimental data set, ANN model architecture development, construction and testing of the ANN model, and prediction.
2. The predicted CGRs obtained from the trained ANN are in good agreement with the experimental data that were used for evaluation purposes. The ANN reproduced some well-known nonlinear interactions among the variables of interest ( $T$ ,  $K_I$ , Yield strength, B content, Li content, ECP and pH).

3. A sensitivity analysis based on the use of “fuzzy curves” ascertained the contributions of the various independent variables to determining the crack growth rate and hence the “character” of the phenomena determining the dependent variable (CGR). This analysis indicates that temperature is the most important factor in determining CGR, followed by  $K_I$ , ECP, conductivity, [LiOH], pH, Yield Strength, and  $[H_3BO_3]$  in that decreasing order. The mechanical factor ( $K_I$ ) and the principal electrochemical factor (ECP) both have a major impact on CGR, with  $K_I$  being slightly more important. It is this reason that we classify crack growth in Alloy 600 as being “electrochemically-enhanced mechanical” in character.
4. The successful development of the ANN for making CGR predictions from experimental data provides a powerful tool for predicting CGR in PWR primary coolant in operating Pressurized Water Reactors.

## Acknowledgements

The authors gratefully acknowledge the financial support from the National Key Basic Research Program of China (Nos. 2011CB610505 and 2014CB046801), Specialized Research Fund for the Doctoral Program of Higher Education (20120032110029). Jiangbo Shi also thanks the China Scholarship Council for supporting his study abroad.

## Appendix A. Supplementary material

Supplementary data associated with this article can be found, in the online version, at <http://dx.doi.org/10.1016/j.corsci.2014.12.007>.

## References

- [1] P.M. Scott, An analysis of primary water stress corrosion cracking in PWR steam generators, in: Proc. of the Specialists Meeting on Operating Experience with Steam Generators, Brussels, Belgium, 1991, pp. 5–6.
- [2] Hicking, A. McIlree, R. Pathania, Crack Growth Rates for Evaluating Primary Water Stress Corrosion Cracking (PWSCC) of Thick-Wall Alloy 600 Material (MRP-55), Electric Power Research Institute, Palo Alto, 2002. NRC ADAMS Accession No. ML023010510.
- [3] Materials Reliability Program Crack Growth Rates for Evaluating Primary Water Stress Corrosion Cracking (PWSCC) of Alloy 82, 182, and 132 Welds (MRP-115), EPRI, Palo Alto, CA, 1006696, 2004.
- [4] Program on Technology Innovation: Prediction and Evaluation of Environmentally Assisted Cracking in LWR Structural Materials, EPRI, Palo Alto, CA, EDF-SEPTEN, Hitachi Ltd., Japan Atomic Power Company, Kansai Electric Power Co., Inc, Mitsubishi Heavy Industries Ltd, Swedish Radiation Safety Authority, Tohoku Electric Power Co. Inc, Tokyo Electric Power Company, Toshiba Corporation, Ishikawajima-Harima Heavy Industries Co. Ltd, and Tohoku University, 1019034, 2009.
- [5] D.D. Macdonald, M. Urquidi-Macdonald, A coupled environment model for stress corrosion cracking in sensitized Type 304 stainless steel in LWR environments, *Corros. Sci.* 32 (1991) 51–81.
- [6] D.D. Macdonald, M. Urquidi-Macdonald, An advanced coupled environment fracture model for predicting crack growth rates, in: Parkins Symposium on Fundamental Aspects of Stress Corrosion Cracking, 1991, pp. 443–455.
- [7] H.S. Kim, A Study for Modeling Electrochemistry in Light Water Reactors, The Pennsylvania State University, 2007.
- [8] D.D. Macdonald, Viability of hydrogen water chemistry for protecting in-vessel components of boiling water-reactors, *Corrosion* 48 (1992) 194–205.
- [9] D.D. Macdonald, P.C. Lu, M. Urquidi-Macdonald, The use of neural networks in the prediction of damage in water cooled nuclear reactors, in: Proc. Int'l. Symp. on Plant Aging and Life Prediction of Corrodible Structures/95, NACE International, Houston, TX, 1995, pp. 1–7.
- [10] P.-C. Lu, The deterministic and nondeterministic models for the prediction of crack growth rates in Type 304 SS, in: Engineering Science and Mechanics, Pennsylvania State University, 1994, pp. 1–274.
- [11] J.P. Cai, R.A. Cottis, S.B. Lyon, Phenomenological modelling of atmospheric corrosion using an artificial neural network, *Corros. Sci.* 41 (1999) 2001–2030.
- [12] S. Pintos, N.V. Queipo, O.T. de Rincon, A. Rincon, R. Morcillo, Artificial neural network modeling of atmospheric corrosion in the MICAT project, *Corros. Sci.* 42 (2000) 35–52.
- [13] M. Halama, K. Kreislova, J. Van Lysebettens, Prediction of atmospheric corrosion of carbon steel using artificial neural network model in local geographical regions, *Corrosion* 67 (2011). 065004–065001–065004–065006.
- [14] H.M.G. Smets, W.F.L. Bogaerts, SCC analysis of austenitic stainless-steels in chloride-bearing water by neural network techniques, *Corrosion* 48 (1992) 618–623.
- [15] M. Benhaim, D.D. Macdonald, Modeling geological brines in salt-dome high-level nuclear waste isolation repositories by artificial neural networks, *Corros. Sci.* 36 (1994) 385–393.
- [16] A. Aleboyeh, M.B. Kasiri, M.E. Olya, H. Aleboyeh, Prediction of azo dye decolorization by UV/H<sub>2</sub>O<sub>2</sub> using artificial neural networks, *Dyes Pigments* 77 (2008) 288–294.
- [17] R. Rebak, A. McIlree, Z. Szklarska-Smialowska, Effects of pH and stress intensity on crack growth rate in Alloy 600 in lithiated+ borated water at high temperatures, in: Proc. Fifth Int. Symp. Environmental Degradation of Materials in Nuclear Power Systems-Water Reactors, 1991, pp. 511–517.
- [18] R. Rebak, Z. Szklarska-Smialowska, Influence of stress intensity and loading mode on intergranular stress corrosion cracking of alloy 600 in primary waters of pressurized water reactors, *Corrosion* 50 (1994) 378–393.
- [19] R.G. Lott, R.J. Jacko, R.E. Gold, Primary water stress corrosion crack growth rates in alloy 600 steam generator tubing, in: Fifth International Symposium on Environmental Degradation of Materials in Nuclear Power Systems-Water Reactors, Monterey, California, 1991, pp. 525–532.
- [20] D. Morton, S. Attanasio, G. Young, Primary water SCC understanding and characterization through fundamental testing in the vicinity of the Ni/NiO phase transition, in: Proc. 10th Int. Symp. on Environmental Degradation of Materials in Nuclear Power Systems-Water Reactors, NACE, 2002.
- [21] PWSCC of Alloy 600 Materials in PWR primary System Penetrations, EPRI, Palo Alto, CA, TR-103696, 1994.
- [22] Crack Growth and Microstructural Characterization of Alloy 600 Head Penetration Materials, EPRI, Palo Alto, CA, TR-105958, 1995.
- [23] Crack Growth and Microstructural Characterization of Alloy 600 PWR Vessel Head Penetration Materials, EPRI, Palo Alto, CA, TR-109136, 1997.
- [24] Materials Reliability Program (MRP) Crack Growth Rates for Evaluating Primary Water Stress Corrosion Cracking (PWSCC) of Thick-Wall Alloy 600 Materials (MRP-55) Revision 1, EPRI, Palo Alto, CA, 1006695, 2002.
- [25] W.E. Ruther, W.K. Soppet, T.F. Kassner, Corrosion Fatigue of Alloys 600 and 690 in Simulated LWR Environments, NUREG/CR-6383, ANL-95/37, 1996.
- [26] D.D. Macdonald, On the modeling of stress corrosion cracking in iron and nickel base alloys in high temperature aqueous environments, *Corros. Sci.* 38 (1996) 1003–1010.
- [27] Materials Reliability Program (MRP) Crack Growth Rates for Evaluating Primary Water Stress Corrosion Cracking (PWSCC) of Thick-Wall Alloy 600 Materials (MRP-55) Revision 1.
- [28] J. Shi, J. Wang, D.D. Macdonald, Prediction of crack growth rate in Type 304 stainless steel using artificial neural networks and the coupled environment fracture model, *Corros. Sci.* 89 (2014) 69–80.
- [29] R.A. Cottis, Q. Li, G. Owen, S.J. Gartland, I.A. Helliwell, M. Turega, Neural network methods for corrosion data reduction, *Mater. Des.* 20 (1999) 169–178.
- [30] A.H. Sung, Ranking importance of input parameters of neural networks, *Expert Syst. Appl.* 15 (1998) 405–411.
- [31] S. Sim, M.K. Cavanaugh, P. Corrigan, I.S. Cole, N. Biribilis, Aqueous corrosion testing and neural network modeling to simulate corrosion of supercritical CO<sub>2</sub> pipelines in the carbon capture and storage cycle, *Corrosion* 69 (2013) 477–486.
- [32] N. Biribilis, M.K. Cavanaugh, A.D. Sudholz, S.M. Zhu, M.A. Easton, M.A. Gibson, A combined neural network and mechanistic approach for the prediction of corrosion rate and yield strength of magnesium-rare earth alloys, *Corros. Sci.* 53 (2011) 168–176.
- [33] G. Kumar, R.G. Buchheit, Use of artificial neural network models to predict coated component life from short-term electrochemical impedance spectroscopy measurements, *Corrosion* 64 (2008) 241–254.
- [34] Y.H. Lin, G.A. Cunningham, A new approach to fuzzy-neural system modeling, *IEEE Trans. Fuzzy Syst.* 3 (1995) 190–198.
- [35] P.L. Andresen, M.M. Morra, Stress corrosion cracking of stainless steels and nickel alloys in high-temperature water, *Corrosion* 64 (2008) 15–29.
- [36] E. Hunt, D. Gross, PWSCC of Alloy 600 Materials in PWR Primary System Penetrations, EPRI Report TR-103696, 1994.
- [37] G. White, J. Hicking, L. Mathews, Crack growth rates for evaluating PWSCC of thick-wall alloy 600 material, in: Proc. of the 11th Intl. Symp. on Environmental Degradation of Materials in Nuclear Power Systems-Water Reactors, NACE International, Houston, TX, 2003, pp. 166–179.
- [38] J. Shi, J. Wang, D.D. Macdonald, Prediction of crack growth rate in Type 304 stainless steel using artificial neural networks and the coupled environment fracture model, *Corros. Sci.* (2014).
- [39] Y. Shen, P.G. Shewmon, intergranular stress-corrosion cracking of alloy 600 and X-750 in high-temperature deaerated water steam, *Metall. Trans. A* 22 (1991) 1857–1864.
- [40] R.B. Rebak, Z. Xia, Z. Szklarska-Smialowska, Effect of temperature and cold work on the crack-growth rate of alloy-600 in primary water, *Corrosion* 51 (1995) 689–697.
- [41] W.C. Moshier, C.M. Brown, Effect of cold work and processing orientation on stress corrosion cracking behavior of alloy 600, *Corrosion* 56 (2000) 307–320.
- [42] T. Terachi, T. Yamada, T. Miyamoto, K. Arioka, SCC growth behaviors of austenitic stainless steels in simulated PWR primary water, *J. Nucl. Mater.* 426 (2012) 59–70.

- [43] T. Cassagne, A. Gelpi, Crack growth rate measurements on alloy 600 steam generator tubing in primary and hydrogenated AVT water, in: Sixth International Symposium on Environmental Degradation of Materials in Nuclear Power Systems–Water Reactors, 1993, pp. 679–686.
- [44] M.O. Speidel, R. Magdoswki, Stress corrosion cracking of nickel base alloys in high temperature water, in: Proceedings of the Sixth International Symposium on Environmental Degradation of Materials in Nuclear Power Systems–Water Reactors, 1993.
- [45] M.M. Hall Jr., W.C. Moshier, D.J. Paraventi, Hydrogen assisted fracture model predictions for alloy 600 PWSCC: sensitivities of crack growth rate to applied stress intensity factor, temperature, carbon concentration, yield stress and crack growth orientation and coolant-borne hydrogen, in: T.S. Mintz, W.H. Cullen (Eds.), Proceedings of the Conference on Vessel Penetration Inspection, Crack Growth and Repair, U. S. Nuclear Regulatory Commission, Gaithersburg Marriott at Washington Center, Gaithersburg, MD, 2005, pp. 745–766.
- [46] P.L. Andresen, T.M. Angeliu, R.M. Horn, W.R. Catlin, L.M. Young, Effect of deformation on SCC of unsensitized stainless steel, *Corrosion* 2000 (2000).
- [47] T. Shoji, G. Li, J. Kwon, S. Matsushima, Z. Lu, Quantification of yield strength effects on IGSCC of austenitic stainless steels in high temperature water, in: Proc. 11th Int. Conf. Environ. Degradation of Materials in Nuclear Power Systems–Water Reactors, ANS, 2003, pp. 834–843.
- [48] M.C. Marin, M.G. Redondo, G. de Diego Velasco, D.G. Briceno, Crack growth rate of hardened austenitic stainless steels in BWR and PWR environments, in: Proc. 11th Int. Symp. Environ. Degradation of Materials in Nuclear Power Systems–Water Reactors, 2003, pp. 845–854.
- [49] W.C. Moshier, D.J. Paraventi, Alloy 600 growth rate testing, in: Workshop on cold work in Iron- and Nickel-Base Alloys, Toronto, Ontario, 2007.
- [50] P.L. Andresen, Similarity of cold work and radiation hardening in enhancing yield strength and SCC growth of stainless steel in hot water, *Corrosion* 2002 (2002).
- [51] P.L. Andresen, L.M. Young, R.M. Horn, P.W. Emigh, Stress corrosion crack growth rate behavior of Ni Alloys 182 and 600 in high temperature water, *Corrosion* 2002 (2002).
- [52] R.A. Mayville, T.J. Warren, P.D. Hilton, The Crack Velocity- $K_I$  Relationship for AISI 4340 in Seawater under Fixed and Rising Displacement, American Society for Testing and Materials, Philadelphia, 1989.
- [53] P.M. Scott, An analysis of primary water stress corrosion cracking in PWR steam generators, in: Proc. Nuclear Energy Agency (NEA)/Committee on the Safety of Nuclear Installations (CSNI)—UNIPED Specialist Meeting on Operating Experience with Steam Generators, NEA/CSNI, Brussels, Belgium, 1991.
- [54] Materials Reliability Program (MRP) Crack Growth Rates for Evaluating Primary Water Stress Corrosion Cracking (PWSCC) of Thick-Wall Alloy 600 Materials (MRP-55) Revision 1, EPRI, Palo Alto, CA: 1006695, 2002.
- [55] P.L. Andresen, M.M. Morra, P.W. Emigh, Effects of PWR primary water chemistry and deaerated water on SCC, *Corrosion* 2005 (2005).
- [56] H. Kim, D.D. Macdonald, Measurement of steady-state hydrogen electrode reactions on Alloys 600 and 690 tubes, *Corros. Sci.* 52 (2010) 1139–1145.
- [57] Z. Szklarska-Smialowska, Z. Xia, R. Valbuena, Mechanism of crack growth in alloy 600 in high-temperature deaerated water, *Corrosion* 50 (1994) 676–681.
- [58] W. Ruther, W. Soppett, T. Kassner, Corrosion fatigue of Alloys 600 and 690 in simulated LWR environments, in: Nuclear Regulatory Commission, Div. of Engineering Technology, Washington, DC, United States, 1996.
- [59] S. Le Hong, J.-M. Boursier, C. Amzallag, J. Daret, Measurement of stress corrosion cracking growth rates in weld alloy 182 in primary water of PWR, in: Proc. Tenth Intl. Conf. on Environmental Degradation of Materials in Nuclear Power Systems–Water Reactors, NACE International, Houston, TX, 2001.
- [60] S.A.M. Attanasio, S. David, Measurement of the nickel/nickel oxide transition in Ni–Cr–Fe alloys and updated data and correlations to quantify the effect of aqueous hydrogen on primary water SCC, in: 11th Int. Conf. Environmental Degradation of Materials in Nuclear Systems, Stevenson, WA, USA, 2003, pp. 143–155.